Vivid Structural Coloration in Transparent MXene-Cellulose Nanocrystals Composite Films

Botyo Dimitrov[1*], Valeriia Poliukhova[1*], Claire Joo[1], Madeline Buxton[1], Irina Roslyk[2], Yury Gogotsi[2], Jacob Crossno[3,4], Kirt A. Page[3,4], Hilmar Koerner[3], Dhriti Nepal[3], Michael E. McConney[3], Timothy J. Bunning[3*], Vladimir V. Tsukruk[1*]

[1] School of Materials Science and Engineering, Georgia Institute of Technology, Atlanta, Georgia 30332-0245, United States

[2] Drexel Nanomaterials Institute and Department of Materials Science and Engineering, Drexel University, Philadelphia, Pennsylvania 19104, United States

[3] Materials and Manufacturing Directorate, Air Force Research Laboratory, Wright-Patterson Air Force Base, Dayton, Ohio 45433, United States

[4] UES A BlueHalo Company, Dayton, OH 45432, United States

*authors contributed equally

*corresponding author

Abstract

In this work, shear-printed layered photonic films with vivid structural coloration were fabricated using an alternation of submicron bio-derived cellulose nanocrystals layers and 2D $Ti_3C_2T_x$ MXene nanoflake layers, which are highly oriented in a parallel manner to the substrate. These ultrathin films (700-1500 nm) showed light transmittance of above 40% in the visible range. In contrast, in reflectance mode, the films appeared vivid colored and iridescent due to distinct photonic bandgaps in the visible and the NIR ranges, rarely observed CNC composites. The violet-to-orange structural coloration can be controlled by the stacking of MXene nanoflakes in nanoscale thin layers separated by thicker cellulose nanocrystals matrix, as confirmed by photonic simulations. The unique combination of distinctly different optical appearance in transmittance and reflectance modes occurred within only a few hybrid MXene-cellulose nanocrystals bilayers due to the molecularly smooth interfaces and high refractive contrast between bio-based and inorganic phases, resulting in a concurrence of constructive and destructive interference. These lamellar biophotonic films open the possibilities for advanced radiative cooling, camouflaging, multifunctional capacitors, and optical filtration applications, while the cellulose nanocrystals matrix strengthens their flexibility, robustness and facilitates sustainability.

Keywords: structural colors, iridescence, transparent film, MXene composites, cellulose nanocrystals, ultrathin photonic films

TOC

Vivid structural coloration in reflectance and high transparency in transmittance modes are observed in biopolymer-layered composite films. The ultrathin multilayered structures with unique optical appearance, near-infrared bandgap, and strong optical reflection with high refractive index contrast caused by alternating MXene and cellulose layers with.

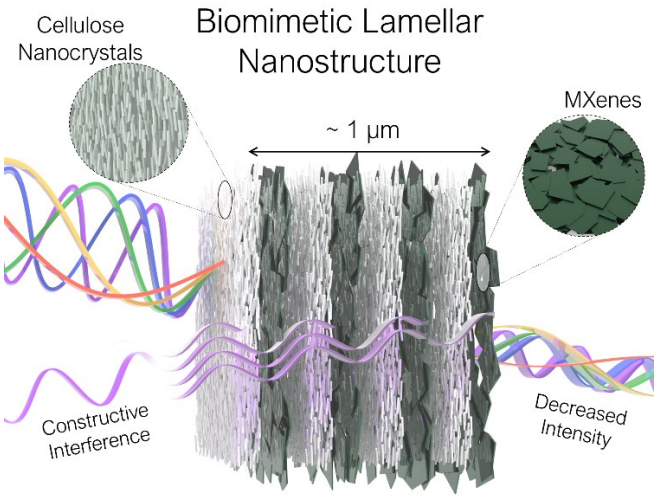

1 Introduction

Biological photonic crystals are ubiquitous among living organisms, with structural coloration serving for protection, communication, and camouflaging.[1,2,3,4] The simplest photonic materials are layered periodic (lamellar) structures based on two optically contrasting phases, widely known as one-dimensional photonic materials (so called Bragg stacks), and they are common for both biological and man-made fabricated materials.[5] Although the optical properties of these photonic materials have been described theoretically long ago, the soft matter-based materials have drawn much attention recently because of their potential for stimuli-responsive behavior and color actuation.[6,7,8]

Lamellar materials can be produced by step-by-step methods in accessible processing conditions, which highly pertinent for large areas[9,10,11] with applications encompassing photonic sensing,[12] photovoltaics,[13] capacitors,[14] and displays.[15] However, because optical applications are often subjected to high-intensity illumination (e.g., in interference optical filters), the biological and organic components might experience photo-bleaching and photodegradation.[16] Thus, optical materials based solely on soft materials often lack long-term durability and sufficiently high optical contrast.[17,18] Thus, searching for new environmentally friendly components with greater refractive index contrast, thermal and photostability is critically important.[3]

Inspired by the naturally occurring lamellar structures, a common biomimetic strategy for fabricating 1D photonic stacks is to alternate organic and inorganic phases (e.g., polymers and nanoparticles) to maximize the refractive index contrast.[19] Among the recently emerging high-index components are the two-dimensional (2D) MXenes, which also have a significant photothermal conversion ability, photostability, and thermal insulation properties.[20,[21,22] MXene flakes with ~1 nm thickness and several μm lateral dimensions possess excellent mechanical properties.[23] The negative permittivity and low emissivity of MXenes in the mid-IR range make them suitable for thermal camouflage[24,25] and radiative heating/cooling.[26] However, some MXenes, such as the most frequently used $Ti_3C_2T_x$, absorb light in the visible and near-infrared (NIR) ranges, rendering them opaque when assembled in several micron-thick films.[21,27]

To date, MXene materials are explored as a component for the fabrication of diverse functional polymeric materials.[28,29] Composite MXene films with different matrices are attractive for

biomedical applications,[30] catalysis,[31] and transparent electron transport layers for photovoltaic and optoelectronic applications.[32,33]

As a promising matrix for advanced photonic composites, nanocellulose materials such as cellulose nanocrystals (CNCs) and cellulose nanofibers (CNFs) are widely considered.[8] CNCs and CNFs are renewably sourced and have the potential for physical modifications.[34] Self-assembled CNC films have shown strong structural coloration, pronounced iridescence, and circular polarization properties caused by a peculiar helical organization with sub-micron pitch length.[35,36,37] Additionally, nanocellulose materials are transparent in the visible range and show excellent mechanical properties[38] applicable to a variety of functional materials.[,39] Recently, the layer-by-layer shear-printing of lyotropic CNC suspensions has been exploited for fabrication of highly uniform twisted structures yielding clear transparent CNC films with pre-programmed twisting angle, handedness, high orientational order, photonic bandgaps, and circular polarization reflection.[40,41]

In this work, we demonstrated novel multilayered ultrathin composite films with a CNC matrix and MXene interlayers (**Figure 1**).

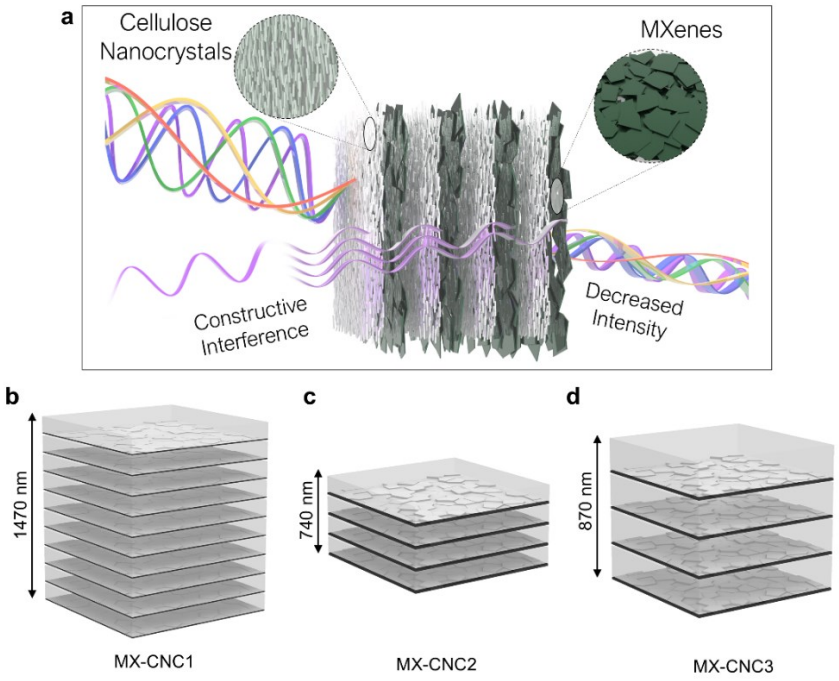

Figure 1. MXene-CNC multilayered films with narrowband reflectance, structural coloration, and high transmittance (a). Three types of films with different thicknesses and numbers of MXene-CNC bilayers are studied here: 10 bilayers in MX-CNC1 (b), 4 bilayers in MX-CNC2 (c), and 4 bilayers in MX-CNC3 (d).

These films show a unique combination of high transmittance and selective strong light reflectance in the visible range and the non-trivial, rarely achieved near-IR spectral region for CNC composites. These superior optical properties result from the pre-defined stacking of the highly oriented flakes in the nm-thin MXene layers with high refractive index and low scattering, which have rarely been observed in conventional composites. Because of the extremely high refractive index contrast between the well-separated organic and inorganic phases, these ultrathin hybrid films show a unique combination of vivid structural coloration in reflection mode but are also transparent and show clear appearance in transmittance mode.

2 Results and Discussion

2.1 Multilayer printing of MXene and CNC Layers

The films were fabricated via layered printing on a customized blade coater (**Scheme 1**).[40,41]

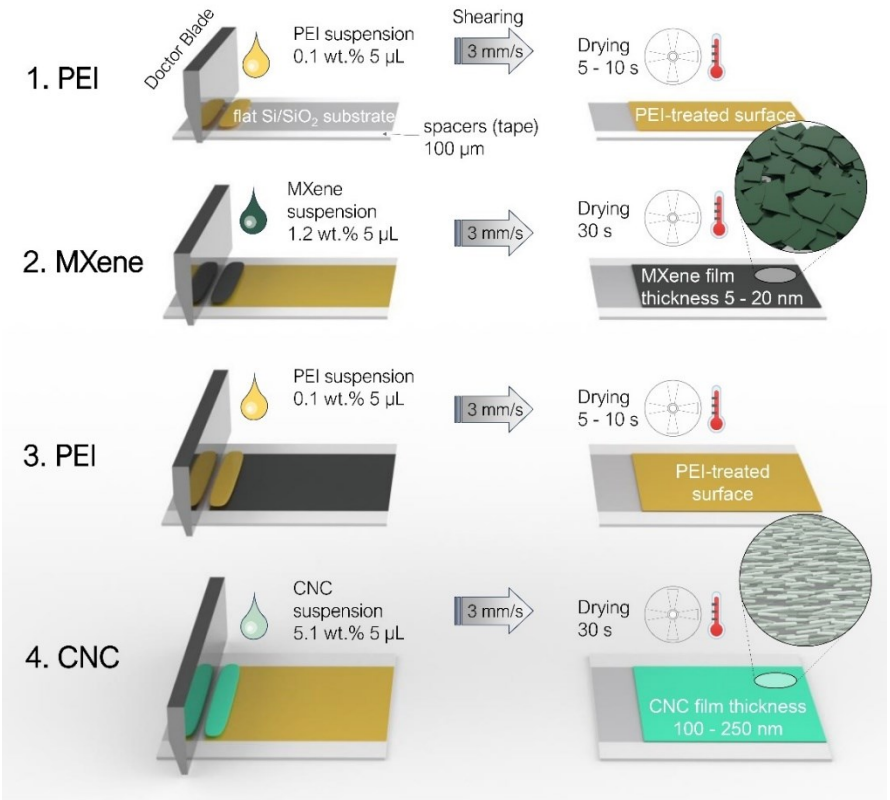

Scheme 1. The MXene-CNC bilayer was constructed by sequential deposition of PEI, MXene, PEI, and CNC layers. First, the dilute PEI suspension was placed on the substrate immediately sheared, and dried with hot air (1). Then, the MXene suspension was deposited on the PEI-treated surface, sheared, and dried to form a layer with a thickness of 5-7 nm (2). In step 3, the PEI was deposited on the MXene layer surface (3). Finally, the CNC suspension was deposited to form a complete bilayer (4). Steps (2) and (4) were repeated to achieve thicker MXene and CNC layers, respectively. To form a complete stack the entire procedure (1-4) was repeated.

Our previous work shows that concentrated CNC suspensions (approximately 5 wt. %) result in films with a thickness of 100-200 nm, with highly aligned CNCs with an orientational order parameter between 0.7 and 0.9 (**Figure 2e**).[40,41] With this fabrication technique, we have demonstrated individual CNC blocks with predefined nanoscale thickness and high birefringence ($\Delta n = 0.07$).

We applied the same method to the MXene nanoflake suspensions to deposit MXene nanolayers on top of a prior-formed CNC layer. The MXene-CNC bilayers fabricated in this manner have been repeated multiple times to form a multilayered stack with tailored number of bilayers (**Scheme 1, Figure S2**). To improve the stability, the CNC film surface was treated with the positively charged polyethyleneimine (PEI) nanoscale-thin layers before the MXene deposition, which resulted in improved block ordering and flake organization as suggested in our previous study.[40]

The atomic-force microscopy (AFM) topography images of the top CNC layer for all films MX-CNC1/2/3 are shown in **Figure 2**. The shear-based printing technique allowed for complete deposition with extremely smooth surfaces and aligned CNCs in the shearing direction with high orientational order, as seen in the high-resolution AFM topography images (**Figure 2d,e,f**). Only a few bundled nanocrystals appeared to be out of the general order of printing, which, however, did not affect the overall reflected colors and the film quality. The CNC layer had a low surface microroughness of below 6 nm as measured within 1x1 μm surface areas with little disturbance of the overall uniformity from the underlying layer of MXene flakes.[42]

In order to analyze the coverage of the MXene nanoflakes on top of the CNC layer, we examined the surface morphology of sequentially deposited MXene layers with AFM phase and topographical imaging (**Figure S2, Figure 3**). When the MXene suspension was shear deposited on a pristine CNC surface, it formed uneven clusters (the darker polygons) with areas of CNC material visible between the clusters (lighter regions) (**Figure S2a,e;b,f;c,g**). In contrast, PEI treatment before MXene deposition drastically improved the nanoflake distribution and orientation, resulting in a smooth layer without agglomerations (**Figure S2d,h**).[42]

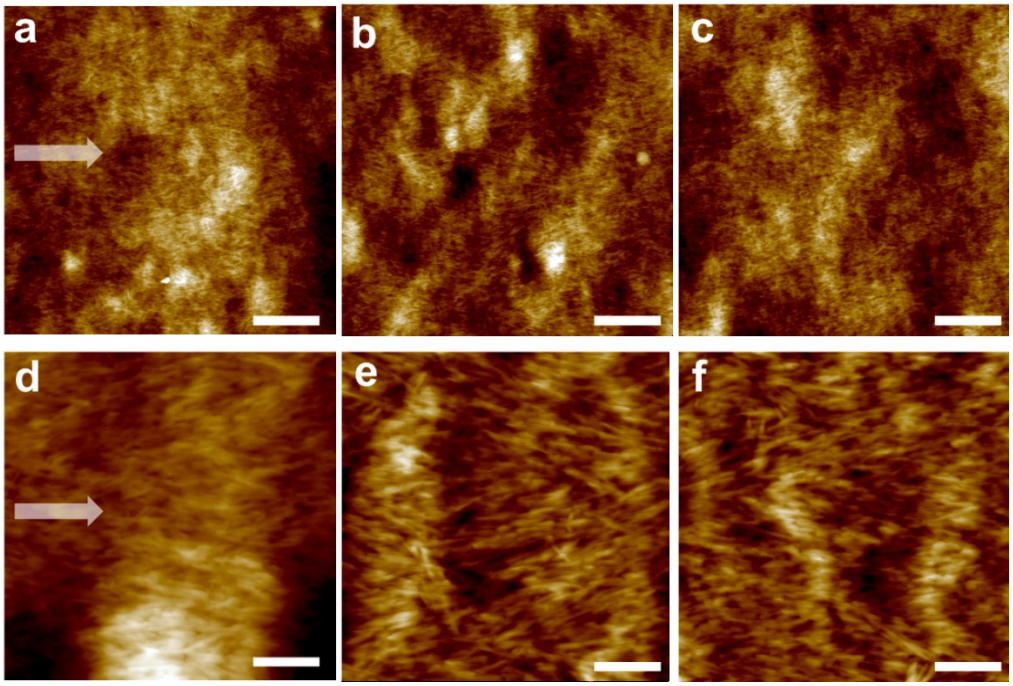

Figure 2. AFM topography 5x5 and 1x1 µm images of top surface of MX-CNC1 (a,d), MX-CNC2 (b,e), and MX-CNC3 (c,f) films of sequential blade-coated MXenes on PEI-treated CNC surface with an arrow indicating the blade-coating direction vector. The Z scale is 40 nm for (a,b,c) and 20 nm for (d,e,f).

To form a thicker MXene layer (up to 20 nm), the shearing procedure was repeated. After three depositions, the flakes were partially folded and creased (**Figure S2j**). However, the creasing didn't significantly impact the overall quality as the surface maintained a low roughness below 11 nm within 10 µm surface areas (**Figure 3b**). Notably, the MXene flakes remain flat and parallel to the CNC surface, a critical factor for overall vertical organization and low-absorbance optical appearance (**Figure S2h,j**).

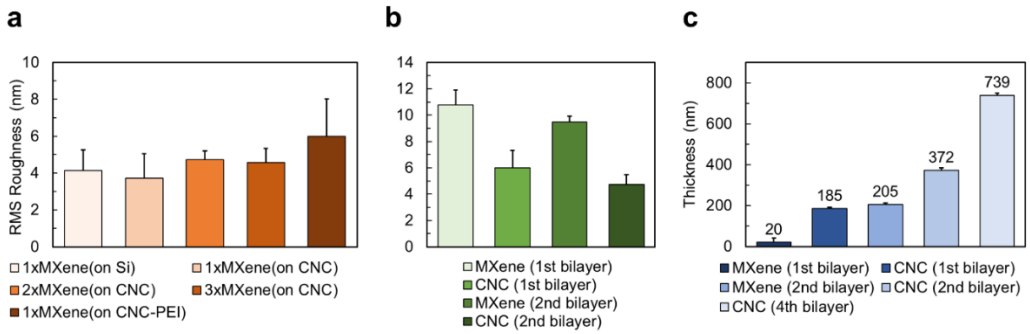

Figure 3. Microroughness measurements of MXene and CNC films. a) Roughness on 10x10 µm regions of MXene deposited on different surfaces. 1x, 2x, 3x indicate the number of MXene depositions. The "on CNC" and "on CNC-PEI" indicate MXene depositions directly on the CNC layer surface and on the PEI-treated surface, respectively. b) Roughness measurements on 1x1 µm regions of a growing stack after MXene and CNC depositions. c) Thickness of the growing stack after sequential MXene and CNC depositions as measured from AFM scratch-test.

2.2 Layered morphology and components alignment

Here, we fabricated three types of MXene-CNC (MX-CNC) films (**Table 1, Figure 1b-d**).

Table 1. MXene-CNC Layered Composite Films. Columns b) and c) show the number of blade coater depositions to form a single MXene and CNC layer, respectively.

	a. # MXene-CNC Bilayers	b. # Depositions per MXene Layer	c. # Depositions per CNC Layer	d. Total Film Thickness (nm)	e. STD (nm)	f. MX-CNC Bilayer Thickness (nm)
MX-CNC1	10	1	1	1470	69	147
MX-CNC2	4	3	1	739	9	185
MX-CNC3	4	3	2	893	23	223

The layer-by-layer printing provided a consistent control in the film thickness (**Figure 3a-d, Figure S3, Experimental Section**). We performed scratch-testing with AFM on the complete MX-CNC1, MX-CNC2, and MX-CNC3 films to obtain the film thicknesses and calculated the individual thickness per bilayer (**Figure S4**). For the MX-CNC2 film, we investigated the thickness with sequential depositions and measured the thickness after every step (**Figure 3c**). The first MXene layer (achieved by 3 repeated shear depositions) was 20 nm thick (**Figure 3c, Figure S3a**). After the next CNC layer was deposited, the total thickness of the MXene-CNC bilayer was measured as 185 nm (thus, 165 nm for the individual CNC layer). This bilayer thickness value was consistent for the following depositions (**Figures 3c; S3b-d**). The film thickness variation with an increasing number of layers showed a highly uniform increment of 185 nm per MXene-CNC bilayer (**Figures 3c, S3**). In the case of the MX-CNC1 film, the MXene-CNC bilayer thickness was lower (147 nm), which was attributed to the single deposition of individual MXene layer.

Next, X-ray diffraction (XRD) measurements were performed to compare the structure of the drop-cast MXene film, CNC film, and the layered MX-CNC1/2/3 films (**Figure 4a-c**). As expected, the pristine CNC film had two broad low-intensity peaks at $2\theta = 15°$ and 22° (**Figure 4a,c**). The peak around 15° with an estimated d-spacing of 5.95 Å is an overlapped diffraction from two crystallographic planes (110) and $(1\bar{1}0)$.[43] The 22° peak corresponds to the (200) planes with a spacing of 3.93 Å. The pristine MXene film showed a characteristic high-intensity and sharp small-angle peak at around $2\theta = 6.95°$ (**Figure 4b**). This peak was attributed to a *d*-spacing of 12.6 Å of the (002) plane of the horizontal stacks of the MXene flakes.[44,45]

In the composite films, we observed peaks at 14.75° and 22.5° attributed to the initial CNC crystalline structure without . The characteristic MXene (002) peak was shifted from 6.95 to 5.8° and 5.9°, indicating an increase in the *d*-spacing to 15.2 Å and 15.0 Å for MX-CNC1/3 and MX-CNC2 films, respectively (**Figure 4b**). This increased spacing can be attributed to the PEI intercalation and partial wrinkling.

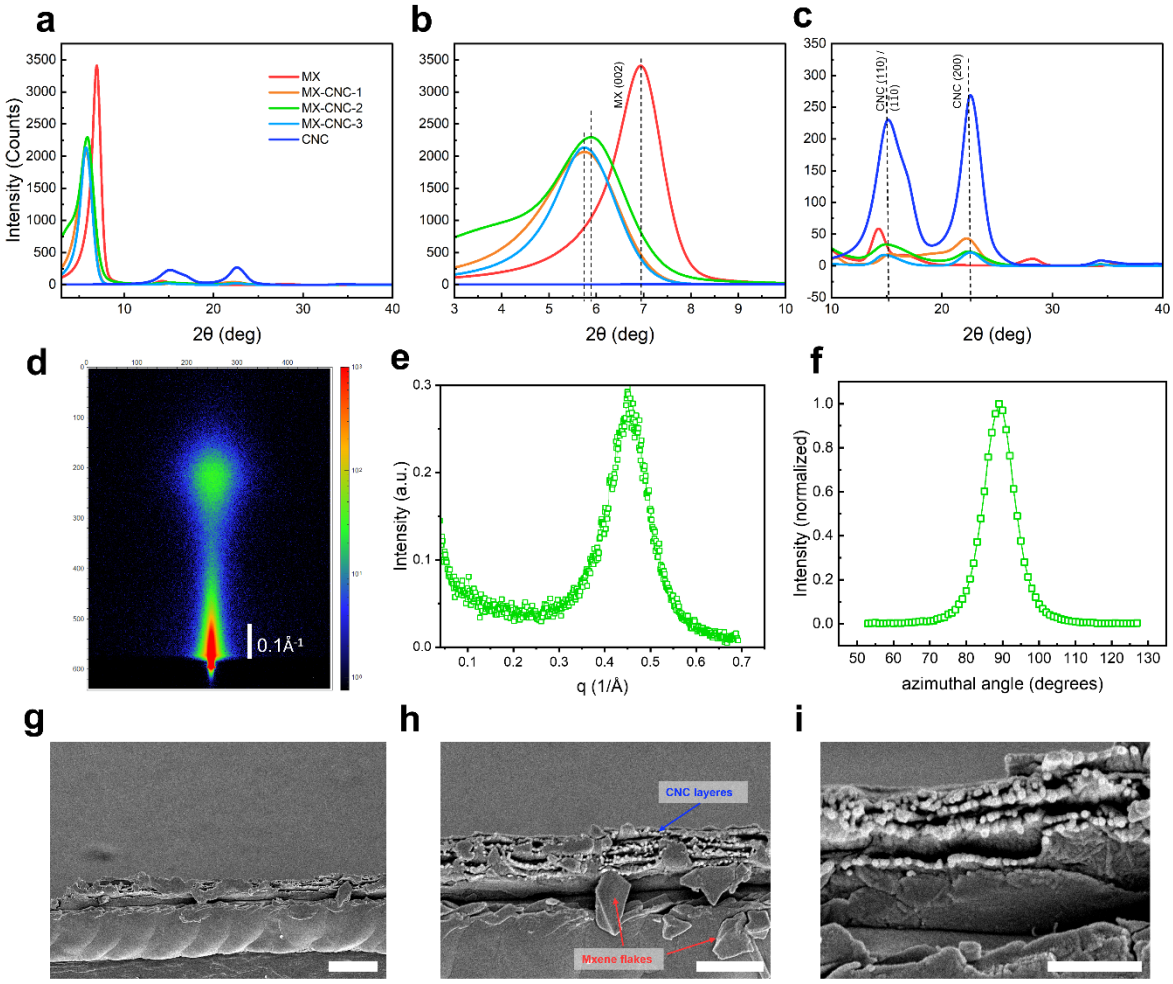

Figure 4. a,b,c) XRD data of MXene, CNC, composite MX-CNC1/2/3 films. The measured angles are plotted in (a). Zoomed-in data is shown for *2θ* 3-10° (b) and 10-40° (c). d,e,f) Grazing incidence X-ray scattering. d) 2D grazing incidence pattern at intermediate angles for MX-CNC2 film; e) intensity versus scattering vector q with (002) diffraction of MXene layer; f) azimuthal intensity distribution of the (002) diffraction peak, which shows a very narrow distribution of flake alignments. g,h,i) Cross-sectional SEM images of the MX-CNC1 film in different magnifications show alternating layers of CNC and MXene. The MXene flakes can be visible from layered delamination in (h). Scale bars for (g), (h), and (i) are 2 µm, 1 µm, and 500 nm, respectively.

Thus, we measured grazing-incidence diffraction of films at wide angles (GiWAXS) for MX-CNC1 and MX-CNC2 (see **Figure S5**). Due to the dominating scattering power of the MXene layers, the MXene contribution was a major component in scattering, with low scattering from

the CNC matrix detected as an quasi-amorphous background. 2D scattering at intermediate angles in GiWAXS is depicted in **Figure 4d-f** for MX-CNC2 as a representative result. The MX-CNC2 exhibits a diffraction peak at ca. 0.45 $Å^{-1}$ directly associated with the (002) plane of the MXene (**Figure 4d**).

Next, flake alignment was estimated by analyzing the (002) peak azimuthal intensity (**Figure 4e-f**). The GiWAXS shows high anisotropy of aligned MXene sheets in the azimuthal intensity distribution with a small disorientation angle of below ±7° (**Figure 4f, S5b**). However, these broader diffraction peaks could be caused by internal MXene structure within the printed MXene layers with some preferential orientation due to the shear-induced deposition.

For quantitative estimation, Herman's Orientation Parameter (HOP) was evaluated from the azimuthal intensity distribution of the (002) MXene diffraction peak according to:[46,47]

$$f = \frac{3\langle \cos^2 \chi \rangle - 1}{2} \qquad (1)$$

The calculated HOP value was -0.48 for the MXene layer, which indicates a nearly perfectly parallel alignment of MXene flakes with respect to the substrate, with 96% of flakes aligned in the preferred horizontal plane. As known, the theoretical value of ideal alignment is -0.5 (see details in the Experimental section).

Finally, scanning electron microscopy (SEM) of film cross-sections confirmed a well-defined lamellar structure of the MX-CNC films (see an example of a 10-bilayer film in **Figures 4g-i**). Indeed, the fractured film showed multiple layers of CNC blocks and horizontal openings with separated MXene layers in between due to film fracturing. Due to delamination and collapse during cross-sectional sample preparation, some of the layers were not clearly visible. Cross-sections of MX-CNC2 and MX-CNC3 films with a larger number of blocks revealed evenly thick layered stacks (**Figure S6**).

2.3 Optical Properties

First, UV-Vis-NIR measurements showed a characteristic broad absorbance peak around 770 nm that indicated an intact chemical composition of the MXene phase.[48] The overall transmittance of the individual 20 nm MXene layer was as high as 90% (**Figure 5a**). The MX-CNC films showed a reduced transmittance down to 30-50% in the visible range and NIR range because of the several incorporated MXene layers with significantly increased total presence of MXene (**Figure 5a**).

It is important to note that periodic peaks became visible in transmittance mode, which otherwise were not observed in the pristine MXene sample (**Figure 5a**). We suggested that these peaks can be attributed to Bragg stack interference in the layered films, which was further confirmed by the reflectance measurements from the UV-Vis and ellipsometry (**Figure 5b,d,e,f**). As well known, this multilayer interference phenomena caused by stacking of layers is commonly observed in lamellar biological materials and gives rise to the distinct vivid coloration in some organisms.[4] The origin of reflected wavelengths is the periodically varying refractive index of the different phases across the film thickness, which results in prohibited light propagation for given wavelengths, effectively forming a photonic bandgap and high reflectance at selected wavelength.[49,50]

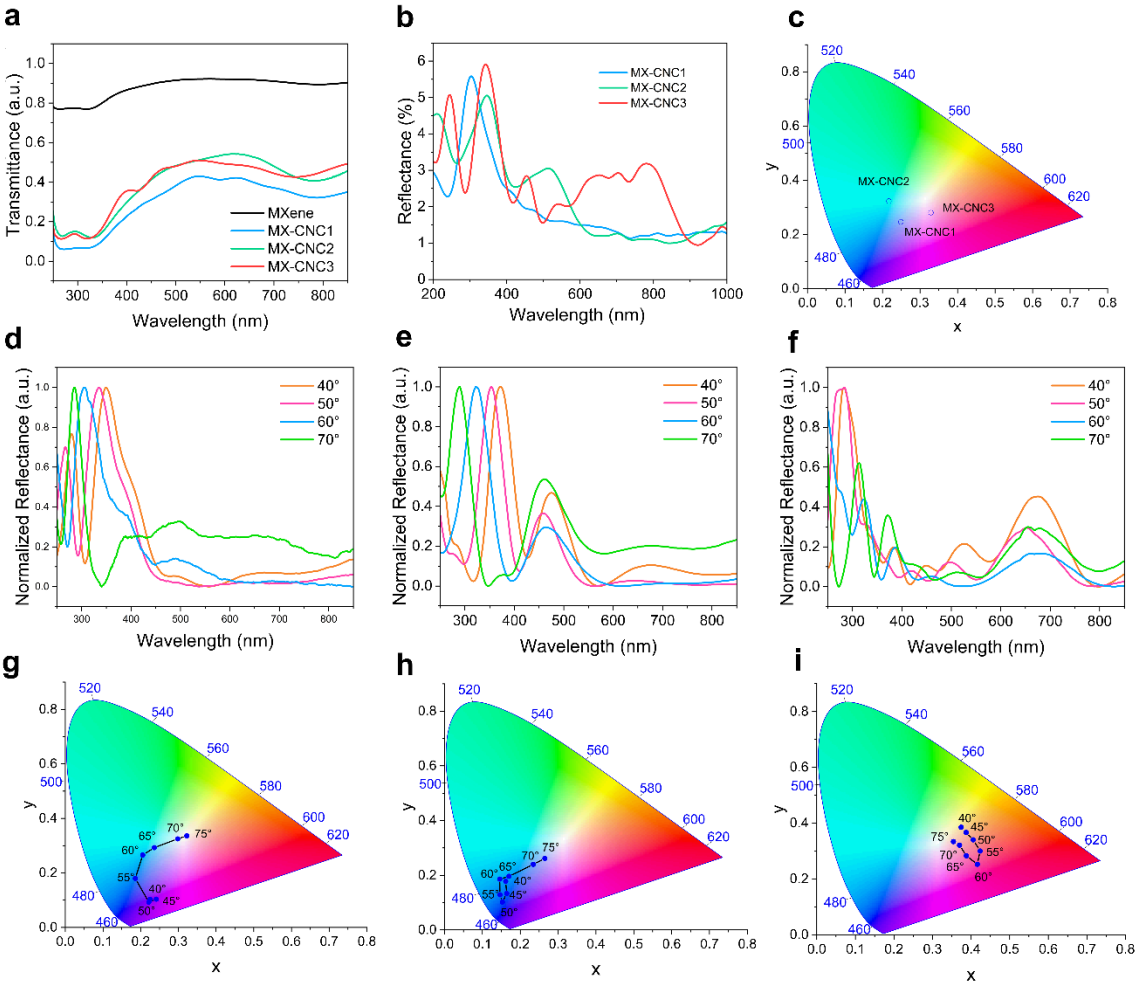

Figure 5. Measured transmittance (a) and reflectance (b) of the MX-CNC films with a UV-Vis-NIR spectrophotometer. CIE 1931 Colorimetric mapping of the composite films (c) based on the reflectance spectra (b). d,e,f) Reflectance measured with ellipsometry at oblique incident angles for MX-CNC1 (d), MX-CNC2 (e), and MX-CNC3 (f) showing blue-shift at increasing angles. CIE 1931 color plots for reflectance spectra of MX-CNC1 (g), MX-CNC2 (h), and MX-CNC3 (i).

In fact, in reflectance mode, all MX-CNC films showed distinct, intense peaks in the ultraviolet, visible, and NIR ranges (**Figure 5b**). The spectrum of the MX-CNC1 film was dominated by a single bandgap near 300 nm. In contrast, the MX-CNC2 film showed two distinct peaks at 350 and 500 nm, while the MX-CNC3 film showed three smaller peaks between 200 and 500 nm and a broad peak at 600-800 nm.

When the reflectance spectra were mapped in the CIE 1931 color space, the MX-CNC1/2/3 films had an appearance with violet-blue, cyan-green, and orange colors, respectively (**Figure 5c**).[51] Colorimetric coordinates were estimated by the convolution of the normalized reflectance with the color-matching functions based on the trichromatic color theory (the Young-Helmholtz theory of color vision).[52,53] Although each spectrum contains several photonic peaks (**Figure 5b**), a single, well-defined color appearance manifests itself in the colorimetric space.

Next, we conducted reflectance measurements of the MX-CNC films at oblique incidence angles. We observed that as the angle increased from 40 to 70°, the reflectance peaks are significantly blue-shifted (**Figure 5d-f**). The shifts were up to 100 nm at lower wavelengths, while the peaks in the red region were less impacted. This trend was clearly visible in **Figure 5d,e** and could also be seen in **Figure 5f,** where the shoulders of the 60° and 70° main peaks were visible near the UV region. The colorimetric mapping based on increasing incidence angles showed corresponding shifts as the reflected color traversed the color space (**Figure 5g-i**). These peak and color shifts indicated an iridescence property that is widely observed in structurally colored natural materials.[17,1] Iridescence also occurs in self-assembled pristine CNC films due to the variation in tactoid orientation and multi-layer interference of helical stacks. However, in our case, the structural coloration and iridescence resulted from Bragg interference of smooth flat layers, which resulted in a very well-defined coloration.[54]

Furthermore, the MX-CNC films were transparent when placed against ambient light on a bright background because of the high film transmittance. Moreover, the films had a remarkable clarity showing a clear image without noticeable hazing (**Figure 6a,b,c**). However, when reflecting a directed light (e.g. from the standard laboratory ceiling lights), the films appeared vividly colored due to the structural color phenomenon as seen in the photographs (**Figure 6d,e,f**). The color change across the film area resulted from the non-uniform film thickness, which was attributed to the preferred directionality during the deposition. In the MX-CNC1/2/3 samples, the colors ranged from violet to orange and red-shifted with increasing

thickness. This trend can also be seen in the colorimetric mapping in **Figure 5c**, in which the calculated colors from the reflectance data matched well the naked eye observations (**Figure 6d,e,f**).

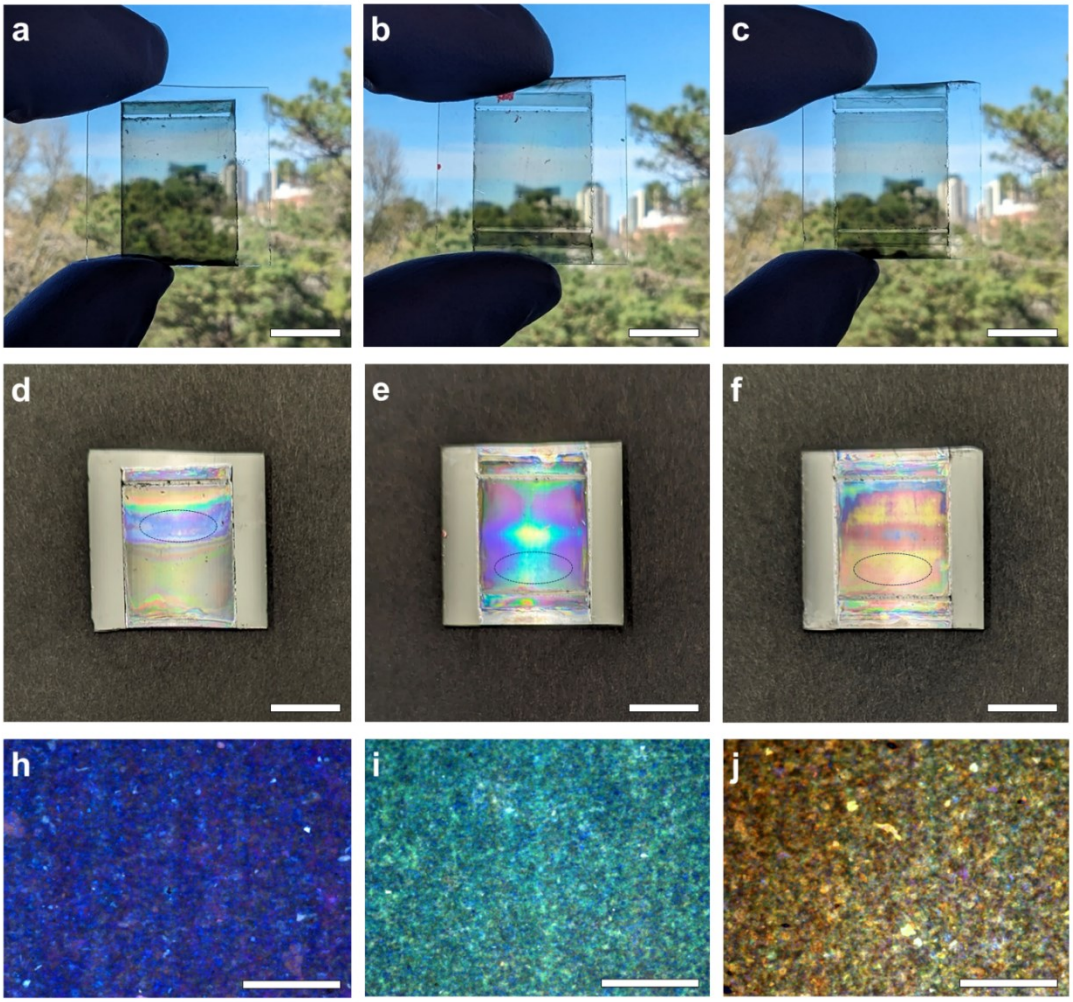

Figure 6. Photographs and optical microscopy images of the films studied here. Left, middle, and right columns correspond to MX-CNC1, MX-CNC2, and MX-CNC3, respectively. a,b,c) The MX-CNC films against ambient light. d,e,f) Appearance of the films, respectively, when placed to reflect ceiling light. h,i,j) Non-polarized OM images of the films, respectively. The black ellipses indicate to locations of the UV-Vis-NIR measurements. Scale bars for (a-f) are 1 cm, and for (h-j) are 100 μm.

Bright-field optical microscopy in reflectance mode also showed vivid coloration of the films (**Figures 6h-j, S7, S8**). The films appeared specular at greater magnifications (50x and 100x objective lenses) due to the diverse polygonal shapes of the flakes (**Figures 6h-j, S7**). With increasing depth some of the nanoflakes appeared to be darker due to the partial absorbance from the upper MXene layers, in contrast to the brightly colored shapes from the upper layers. This difference in the shapes and colors can be an opportunity for applications in anti-

counterfeiting (e.g. physical unclonable function).[39] Despite the polydispersity on the µm scale, the films possessed very well-defined coloration and clarity with narrow bandgaps and minimal interfacial scattering within a minimal thickness, in contrast to conventional thicker composite films.[55,56]

It is worth noting that the structural coloration as observed with the naked eye and OM was preserved over six months storage under ambient conditions. This remarkable stability can be attributed to the effective coating of MXene phases by CNC layers within the lamellar morphology that prevents photooxidation processes. Indeed, enhanced stability was demonstrated for Mxene encapsulated in biopolymer layers. [29]

2.4 Photonic Simulations

Based on the results of the lamellar film structure and the measured thicknesses, we developed models for photonic simulations (**Figure S10**). The optical constants for MXene, as obtained from ellipsometry, were consistent with earlier studies (**Figure S9**).[57] The measured refractive index was between 2.0 and 2.3 in the ultra-violet and visible ranges, while the index for the CNC-only film ranged from 1.5 to 1.6. Thus, the index contrast between the two phases was in the range of 0.4-0.8, which is considered to be very high. We used these values to set up the finite-difference time-domain (FDTD) model.

We performed simulations on three scenarios with different stacking periodicity – 150 (a, b, c), 185 (d, e, f), and 220 nm (g, h, i) (**Figures 7, S10**). The lack of pronounced peaks in transmittance could be attributed to the light absorbance by the MXene phase. These results were in close agreement with the experimental reflectance spectra (**Figure 5a**). Indeed, as seen in the E-field distributions, after passing through the film, the intensity for all wavelengths was significantly reduced (**Figure 7b,e,h**). For wavelengths in the region of film bandgaps, the intensity of the field decreased in the depth of the film. Essentially, the contribution to the photonic reflectance of the bandgaps was weaker for deeper layers. Thus, we can suggest that a limited number of nanoscale MXene layers can be used to achieve high reflectance without compromising the high light transmittance.

Our simulations showed that even a few nanoscale MXene layers proved sufficient for sharp reflectance peaks caused by photonic bandgaps because of the high refractive index contrast (**Figure 7a,d,g**). For the 150 nm spacing between MXene layers, two peaks at around 230 and 450 nm appeared (**Figure 7a**) that corresponded to 2nd and 1st orders, respectively (**Figure 7b**). For 185 nm spacing, 1st and 2nd wave orders were possible (**Figure 7e**), and for the 220 nm

spacing, periodicity up to 3rd order was present (**Figure 7h**). These relationships give rise to the complex appearance of two or three photonic bandgaps for films with different layer periodicity and spacing, a unique photonic signature in ultrathin MX-CNC films with a thickness of around 1 μm.

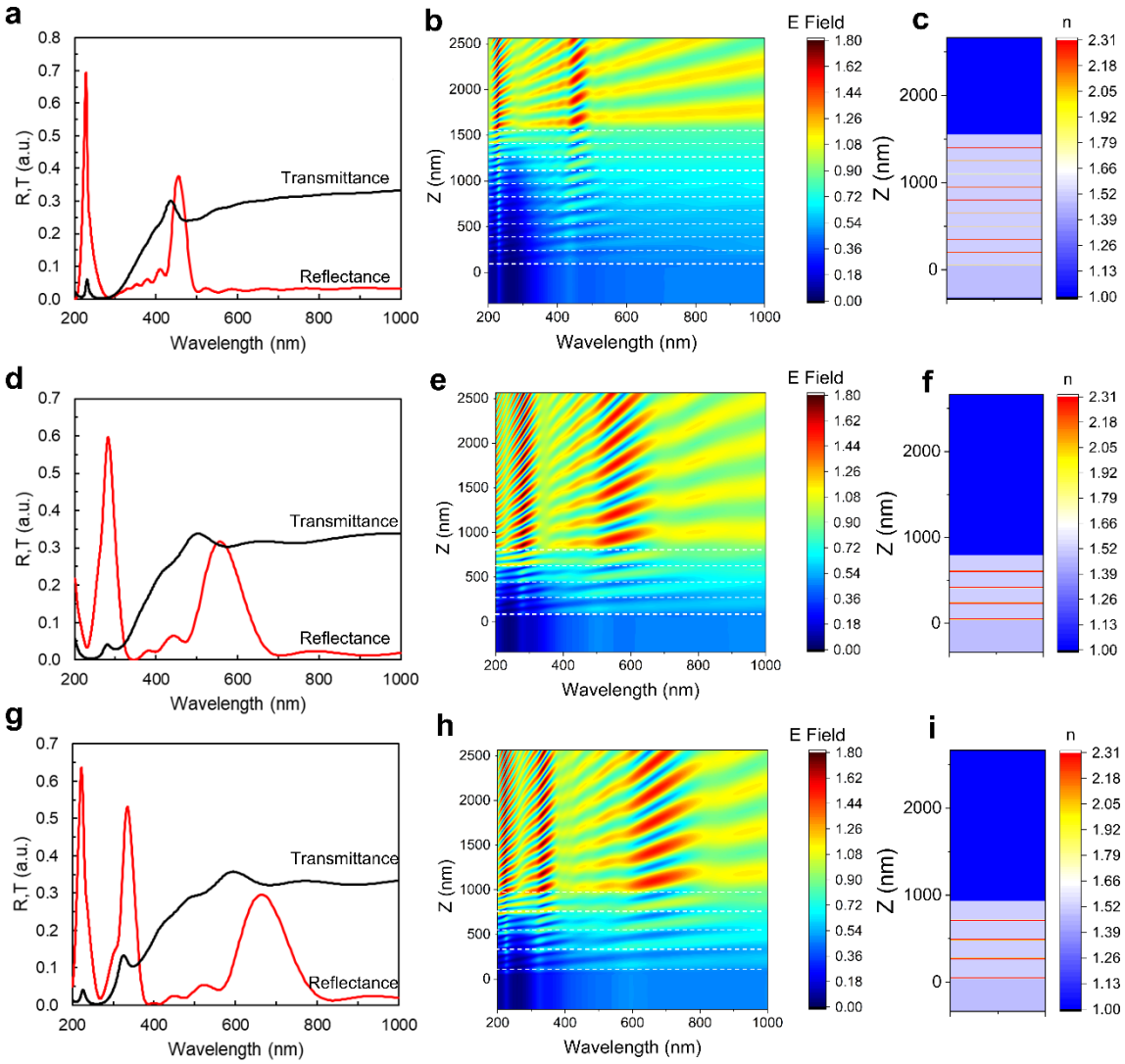

Figure 7. FDTD simulations on bilayer stacks with 150, 185, and 220 nm spacing (first, second, and third row, respectively). a,d,g) Simulated transmittance and reflectance spectra. b,e,h) The E-field plots across the simulated wavelengths (with dashed white lines indicating the positions of the higher-refractive index phase. c,f,i) Refractive index plots.

Furthermore, we evaluated the contribution from constructive interference of the layered structure (**Figure 7b,e,h**)[58] by calculating the position of reflectance peaks for normal incidence:

$$\lambda_c = \frac{2(n_a d_a + n_b d_b)}{m} \quad (2)$$

where λ_c is the bandgap wavelength, n_a and n_b are the refractive indices, d_a and d_b are the physical thicknesses of the respective phases, and m is the order. [59] The calculated peak positions were in reasonable accordance with the simulated reflectance peaks and experimental reflectance (**Figures 5, 7, Table 2**). Both calculated and simulated results are in excellent agreement with the analytical estimations of photonic bandgap appearance for specific designed and experimentally verified morphology lamellar structure. The photonic bandgaps arising from this multilayer structure produce reflectance at highly specific wavelengths, which in turn result in vivid coloration at different viewing angles. These reflectance bandgaps are directly correlated to the thickness d_a and d_b of the lamellae (**Eq. 2**). Smaller spacing d_a + d_b (~150 nm) tends to result in a main peak in the violet-blue region, intermediate spacing (~185 nm) - in the cyan-green region, and the greater spacing (~220 nm) - in the yellow-red region. These, respectively, render violet-blue, cyan-green, and orange-colored films.

Table 2. Calculated reflectance maxima positions (for refractive indices n_a = 1.56 and n_b = 2.1). λ_m is the maximum reflectance wavelength for order m. The calculations and simulations were done with phase thicknesses d_a and d_b for CNC and MXene, respectively.

		d_a (nm)	d_b (nm)	$\lambda_{m=1}$ (nm)	$\lambda_{m=2}$ (nm)	$\lambda_{m=3}$ (nm)
	Calculation	147	3	471	236	N/A
MX-CNC1	Simulation	147	3	460	227	N/A
	Experimental			296	N/A	N/A
	Calculation	175	10	588	294	N/A
MX-CNC2	Simulation	175	10	570	283	N/A
	Experimental			520	348	214
	Calculation	210	10	697	349	232
MX-CNC3	Simulation	210	10	682	338	223
	Experimental			703	347	247

3 Conclusion

This work demonstrated vivid structurally colored ultrathin composite films from highly contrasting phases with high optical transparency (within 30-50%), clear appearance, and strong reflectance with multiple photonic bandgaps. These findings present a unique combination of optical properties for μm-thin biopolymer-based films. Within the lamellar

architecture, the highly refractive and low-roughness nanoscale MXene phase essentially served as a highly reflective mirror separated by transparent CNC layers with submicron thicknesses. Due to the high refractive index difference between the two phases, a strong light reflection and iridescence structural colors caused by Bragg interference were demonstrated for ultrathin films with a very few MXene-CNC stacks.

We showed that disparate refractive materials—natural polymer nanocrystals and 2D titanium carbide flakes—can be assembled through accessible printing processing condition and maintain stable photonic response over months under ambient conditions. These robust layered films could facilitate various unique applications, including optical filters, infrared reflectance films, energy storage, thermal insulation, anti-counterfeiting, and transparent colorful coatings. Moreover, layered design opens interesting avenues in radiative cooling or infrared-visible camouflaging with exceptional combination of selective reflectance, transparency, and stability.

4 Experimental Section

Materials

The delaminated $Ti_3C_2T_x$ MXene flakes were synthesized by selective wet-chemical etching of Al from MAX phase Ti_3AlC_2 produced by Carbon Ukraine, Ltd, with particle size <40 μm. The Ti_3AlC_2 MAX phase was first washed with HCl to remove impurities and then immersed in 20 mL of etchant ($HF:HCl:H_2O$ = 1:6:3) and kept stirring at 35 °C for 24 h. The etchant mixture contained HF (48-51 wt. %, Acros Organics) and HCl (37 wt. %, Fisher Scientific). 1 g of LiCl (99%, Alfa Aesar) per 1 g of etched Ti_3AlC_2 MAX was dissolved in 50 mL of DI water and stirred at 300 rpm at RT for 24 h to obtain delaminated $Ti_3C_2T_x$ MXenes, which was finally washed in DI water and centrifuged at 3500 rpm for 5 min. The delaminated MXenes were redispersed by manual shaking after discarding the supernatant with continuous repletion of the washing cycles until pH 6. The obtained solution was centrifuged at 3500 rpm for 60 min, after which a single to a few layers of MXene were collected.

Single-layer MXene flakes have a thickness of approximately 1 nm, span several microns, and have a polygonal shape (**Figure S1**). The MXene flakes are suspended in water with 1.2 wt. % concentration and vortex-stirred before deposition.

CNC suspension with 5.1 wt. % was used to form the CNC layer of the films. The suspension was prepared via sulfuric acid hydrolysis from bulk delignified wood pulp.[34] The initial hydrolysis procedure yielded a suspension with 0.76 wt. % concentration, which was saturated in an incubator with temperatures varying between 35 and 40°C to facilitate the evaporation of water until the desired concentration was reached.

Sample preparation

Blade coating was used to prepare the films on silicon wafers and SiO_2 glass slides. Blade coater model *TQC Sheen* with a shearing rate of 4 mm s^{-1} was applied for fabrication of ultrathin CNC and MXene layers. In our customized instrument, the original gap in blade sets around several microns and after drying and shearing of suspension dried layers were formed with thickness below 200 nm.

The layered films are fabricated by sequential deposition of MXene and CNC suspensions (Scheme 1). [40] First, the MXene suspension is placed with a pipette on the substrate (Scheme 1.1) and immediately sheared (2). Drying with a heat gun yields a uniform film with a thickness of around 5 nm (3). Next, the CNC suspension is deposited on top of the MXene film (4) and again sheared (5), after which a longer drying time of around 30 seconds is needed to dry the film completely (6). Before each deposition, a PEI suspension is coated using the same procedure. To achieve higher CNC thickness, steps 4-6 are repeated. The procedure can be repeated multiple times to achieve layered films. MX-CNC multilayer films were studied after sequential depositions to establish film thickness growth in the following order: a layer of PEI was deposited initially, followed by depositions of MX, followed by another PEI layer, and ending with a deposition of CNC. Three thin films on silica substrates were produced; the PEI, present in all cases between the MXene and CNC phases, is omitted.

AFM

AFM was performed on a Bruker Dimension Icon instrument. Scans were performed with 5x5 μm and 40x40 μm for surface morphology and 10x10 μm for scratch-test. Nanoscope Analysis 2.0 software was used for post-processing (image flattening and cleaning) and data analysis (depth measurements, step height, surface roughness). Surface microroughness measurements were done on 1x1 and 10x10 μm surface areas. Five data points (regions) from the surface were measured and used for estimating the standard deviation (STD) with the five data points. [42]

Samples were measured in tapping mode at a resolution of 512x512 and 1024x1024 pixels at a rate of 0.5 Hz. The scratch test was done as follows: the suspension (MXene or CNC) is deposited on a silicon substrate according to Scheme 1. Then, a scratch is done with a razor blade to remove part of the film, revealing the substrate surface. AFM height imaging is done on the edge of the film along the scratch to measure the height difference. For the MX-CNC films, the thickness was measured by doing a scratch test after each deposition. The STD was measured after importing the depth histogram in Origin 2022 Pro and fitting a Gaussian function in the peak and STD evaluation.

UV-Vis-NIR

We used a Shimadzu UV-3600 Plus for transmittance measurements in the range of 350-1000 nm. The reflectance spectra of the MX-CNC films on glass were measured using a Shimadzu UV-3600i spectrophotometer equipped with an ISR-603 integrating sphere attachment. The measurements were performed with a stair correction at a 0° incidence angle with a 5 nm slit width across the range of 200 – 1000 nm. Colorimetric mapping was performed on the obtained reflectance spectra for MX-CNC-1,2,3 with the chromaticity diagram plugin to calculate the CIE 1931 coordinates and create the corresponding color visualizations.

Ellipsometry

Spectroscopic ellipsometry and transmittance measurements were performed with a Woollam M-2000U Spectroscopic Ellipsometer. To obtain the best fit, a combination of Drude and two Harmonic Oscillators was used to approximate the *n-k* values, followed by an *n-k* fit for each wavelength. First, the silica glass substrate was fully characterized for transmittance, delta, and psi constants. Then, MXene on silica glass was measured for transmittance, delta, and psi constants. The transmittance and ellipsometric datasets were merged, and a fit for the extinction coefficient and the refractive index were performed in that order. Reflectance was measured at different angles of incidence (40, 50, 60, and 70°). The *p*-polarized source was used, and the Brewster's angle effect can be expected for steep angles.

Optical Microscopy

Non-polarized, linearly-polarized, and cross-polarized OM was performed on an Olympus BX51 microscope in bright-field reflectance mode with 10x/0.30 BD, 50x/0.80 BD, and 100x/0.90 BD Leica MPlanFL N objective lenses, and a total magnification was a 150x, 750x, and 1500x, respectively. The samples on a glass substrate were studied.

FDTD

FDTD simulations were performed with the ANSYS Lumerical (version 2023 R2.1) 3D FDTD software. Materials with 150, 185, and 220 nm bilayer periods were modeled with 3, 10, and 10 nm MXene phases, and 147, 175, and 210 nm CNC phases, respectively. Auto-meshing with Level 3 accuracy was used for the overall FDTD simulation region, and a manual mesh grid with a 0.2 nm step was used for the areas of the MXene layers. The optical constants from the ellipsometric spectroscopy were used to inform the material *n* and *k* constants and to model the MXene and CNC phases.

XRD

XRD analyses of the MX, CNC, and MX-CNC1,2,3 thin films on glass slides were conducted using Rigaku SmartLab XE equipped with a HyPix-3000 2D detector and Cu anode X-ray radiation (wavelength 1.5 Å). The XRD patterns were obtained in parallel beam geometry mode using a 0 background sample holder. Measurements were performed at a scan rate of 1 deg min^{-1} across a 2θ range: 3-60°, with a greasing angle of 0.3. Subsequently, background substruction and calculation of the *d*-spacing were carried out using SmartLab Studio II software.

SEM

SEM images of the MX, CNC, and MX-CNC thin films were obtained using the 8230 FE-SEM equipped with a cold field emission (CFE) gun with secondary electron (SE) detection at 3 kV and a 5-10 mm working distance. The preparation of the samples involved cutting the glass slides with a diamond cutter to achieve clear cross-sections. The samples were then coated with a 10 nm layer of Au:Pd using Q150V Plus Automatic Coater. Following this, the samples were mounted to a 90° SEM stub using carbon tape.

X-ray Scattering

X-ray scattering was performed in the grazing incidence configuration using the Xenocs Xeuss 3.0 SAXS/WAXS system operating at a wavelength of 0.154 nm. Scattering images were acquired using a Pilatus3 R 300K detector and analyzed using the Xenocs XSACT software.

Grazing-incidence scattering was performed on MX-CNC layered films on glass substrates. The scattering was collected at sample-to-detector (STD) distances of 0.06, 0.6 and 1.6 meters. Data for STD of 0.06 is not shown because no additional information was gathered from this

distance. The streak at small angles was captured and illustrates the high degree of alignment of the 2D sheets. The grazing-incidence angle (omega) was set to 0.20°. A schematic of the setup is shown in Figure S7).

The intensity versus scattering vector GiWAXS, obtained from wedge corrected 2D patterns. The diffraction peak around 14Å is caused by diffraction from the interlayer distance between layers within the MXene sheets in MX-CNC2. The intensity versus scattering vector plots in **Figure S5** GiWAXS b) are obtained from wedge-corrected images for GiWAXS (0.06 meters, MX-CNC1 = black, MX-CNC2 = red). Figure S7 GiWAXS c) and d) show the uncorrected 2D GiWAXS patterns for MX-CNC1 and MX-CNC2, respectively.

In addition, the Xeuss XSACT software was used to characterize the degree of orientation via the 2nd order Legendre, or Herman's Orientation Parameter (HOP) for the highly aligned MXene diffraction peak and the azimuthal intensity distribution according to:

$$f = \frac{3\langle \cos^2 \chi \rangle - 1}{2}$$

where

$$\langle \cos^2 \chi \rangle = \frac{\int_{-\frac{\pi}{2}}^{\frac{\pi}{2}} \mathrm{I}(\chi) \cos^2 \chi \sin \chi \, d\chi}{\int_{-\frac{\pi}{2}}^{\frac{\pi}{2}} \mathrm{I}(\chi) \sin \chi \, d\chi}$$

I(χ) is the azimuthal distribution of the scattering intensity. In this scenario, the HOP was determined using the plane of the film as the reference director and the scattering vector, Q, associated with a particular crystallographic plane as the director of interest. The HOP value ranges from -0.5 to 1 where -0.5 indicates that the plane is oriented parallel to the substrate, 0 is random orientation, and 1 is orientation perpendicular to the substrate.

Acknowledgments

This research is supported financially by the Fulbright Bulgarian-American Commission for Educational Exchange, Air Force Office for Scientific Research grant FA9550-23-1-0641, and Air Force Research Laboratory grant FA 8650-22-D5803, NSF-CBET 2202907 Award and the GTNext Award. We would like to thank Dr. Daria Bukharina for providing the measurements of the CNCs dimensions and Sonia Mahjoubi for her help during the initial stages of this work.

Conflict of Interest

The authors declare no conflict of interest

References

[1] P. Vukusic, J. Noyes, in *Bionanotechnology II* (Ed: D. E. Reisner), Taylor & Francis Group, Boca Raton, United States, 1st ed., **2011**, Ch. 25.
[2] O. Karthaus, *Biomimetics in Photonics*, CRC Press, Boca Raton, United States, 1st ed., **2012**.
[3] D. Nepal, S. Kang, K. M. Adstedt, K. Kanhaiya, M. R. Bockstaller, L. C. Brinson, M. J. Buehler, P. V. Coveney, K. Dayal, J. A. El-Awady, L. C. Henderson, D. L. Kaplan, S. Keten, N. A. Kotov, G. C. Schatz, S. Vignolini, F. Vollrath, Y. Wang, B. I. Yakobson, V. V. Tsukruk, H. Heinz, *Nat. Mater.* **2022**, *22*, 18.
[4] R. Xiong, J. Luan, S. Kang, C. Ye, S. Singamaneni, V. V. Tsukruk, *Chem. Soc. Review*, **2020**, *49,* 983
[5] C. P. Barrera-Patino, J. D. Vollet-Filho, R. G. Teixeira-Rosa, H. P. Quiroz, A. Dussan, N. M. Inada, V. S. Bagnato, R. R. Rey-Gonzalez, *Sci. Rep.* **2020**, *10*, 5786.
[6] H. Shen, Z. Wang, Y. Wu, B. Yang, *RSC Adv.* **2016**, *6*, 4505.
[7] J. Jeon, D. Bukharina, M. Kim, S. Kang, J. Kim, Y. Zhang, V. Tsukruk, *Resp. Materials*, **2024,** 2: e20230032
[8] R. Xiong, A. M. Grant, R. Ma, S. Zhang, V. V. Tsukruk, *Mat. Sci. & Eng. Reports*, **2018**, *125*, 1.
[9] M. R. Beaulieu, N. R. Hendricks, J. J. Watkins, *ACS Photonics* **2014**, *1*, 799.
[10] I. R. Howell, C. Li, N. S. Colella, K. Ito, J. J. Watkins, *ACS Appl. Mater. Interfaces* **2015**, *7*, 3641.
[11] C. Inui, Y. Tsuge, H. Kura, S. Fujihara, S. Shiratori, T. Sato, *Thin Solid Films* **2008**, *516*, 2454.
[12] H. Sayed, M. A. Swillam, A. H. Aly, *Sci. Rep.* **2023**, *13*, 20593.
[13] C. Cetinkaya, E. Cokduygulular, B. Kinaci, F. Guzelcimen, Y. Ozen, N. A. Sonmez, S. Ozcelik, *Sci. Rep.* **2022**, *12*, 11245.
[14] C. Liu, X. Liu, H. Xuan, J. Ren, L. Ge, *Sci. Rep.* **2015**, *5*, 18419.
[15] T. H. Park, S. Yu, J. Park, C. Park, *Sci. Technol. Adv. Mater.* **2023**, *24*, 2156256.
[16] I. Groeneveld, M. Kanelli, F. Ariese, M. R. van Bommel, *Dyes Pigm.* **2023**, *210*, 110999.
[17] D. Kou, S. Zhang, W. Ma, *Adv. Opt. Mater.* **2024**, *12*, 2400192
[18] Z. Wang, C. L. C. Chan, T. H. Zhao, R. M. Parker, S. Vignolini, *Adv. Opt. Mater.* **2021**, *9*, 2100519.
[19] P. Lova, H. Megahd, P. Stagnaro, M. Alloisio, M. Patrini, D. Comoretto, *Appl. Sci.* **2020**, *10*, 4122.
[20] Y. Huang, J. Spiece, T. Parker, A. Lee, Y. Gogotsi, P. Gehring, *ACS Nano* **2024**, *18*, 32491.
[21] D. Zhang, D. Shah, A. Boltasseva, Y. Gogotsi, *ACS Photonics* **2022**, *9*, 1108.
[22] K. Maleski, C. E. Shuck, A. T. Fafarman, Y. Gogotsi, *Adv. Opt. Mater.* **2020**, *9*.
[23] M. Naguib, M. Kurtoglu, V. Presser, J. Lu, J. Niu, M. Heon, L. Hultman, Y. Gogotsi, M. W. Barsoum, *Adv. Mater.* **2011**, *23*, 4248.
[24] L. Li, M. Shi, X. Liu, X. Jin, Y. Cao, Y. Yang, W. Wang, J. Wang, *Adv. Funct. Mater.* **2021**, *31*, 2101381.
[25] M. Han, D. Zhang, A. Singh, T. Hryhorchuk, C. Eugene Shuck, T. Zhang, L. Bi, B. McBride, V. B. Shenoy, Y. Gogotsi, *Mater. Today* **2023**, *64*, 31.
[26] D. Xu, Z. Li, L. Li, J. Wang, *Adv. Funct. Mater.* **2020**, *30*, 2000712.
[27] Y. Li, C. Xiong, H. Huang, X. Peng, D. Mei, M. Li, G. Liu, M. Wu, T. Zhao, B. Huang, *Adv. Mater.* **2021**, *33*, e2103054.
[28] P. Flouda, A. Inman, M. Gumenna, D. Bukharina, V. V. Shevchenko, Y. Gogotsi, V. V. Tsukruk, *ACS Appl. Mater. Interfaces* **2023**, *15*, 53776.
[29] M. C. Krecker, D. Bukharina, C. B. Hatter, Y. Gogotsi, V. V. Tsukruk, *Adv. Funct. Mater.* **2020**, *30*.
[30] H. Lu, J. Wang, H. Li, W. Zhou, Q. Yuan, S. Liu, *Mater. Chem. Front.* **2023**, *7*, 4372.
[31] Á. Morales-García, F. Calle-Vallejo, F. Illas, *ACS Catal.* **2020**, *10*, 13487.
[32] M. A. Saeed, A. Shahzad, K. Rasool, F. Mateen, J. M. Oh, J. W. Shim, *Adv. Sci.* **2022**, *9*, e2104743.
[33] S. Palei, G. Murali, C. H. Kim, I. In, S. Y. Lee, S. J. Park, *Nano-Micro Lett.* **2023**, *15*, 123.
[34] K. Adstedt, E. A. Popenov, K. J. Pierce, R. Xiong, R. Geryak, V. Cherpak, D. Nepal, T. J. Bunning, V. V. Tsukruk, *Adv. Funct. Mater.* **2020**, *30*, 2003597.
[35] O. Kose, A. Tran, L. Lewis, W. Y. Hamad, M. J. MacLachlan, *Nat. Commun.* **2019**, *10*, 510.
[36] H. Zhu, W. Luo, P. N. Ciesielski, Z. Fang, J. Y. Zhu, G. Henriksson, M. E. Himmel, L. Hu, *Chem. Rev.* **2016**, *116*, 9305.

[37] Z. Cheng, Y. Ma, L. Yang, F. Cheng, Z. F. Huang, A. Natan, H. Y. Li, Y. Chen, D. X. Cao, Z. F. Huang, Y. H. Wang, Y. M. Liu, R. D. Yang, H. L. Zhu, *Adv. Opt. Mater.* **2019**, *7*, 1801816.
[38] J. Jaramillo-Fernandez, H. Yang, L. Schertel, G. L. Whitworth, P. D. Garcia, S. Vignolini, C. M. Sotomayor-Torres, *Adv. Sci.* **2022**, *9*, 2104758.
[39] X. Lin, Q. Li, Y. Tang, Z. Chen, R. Chen, Y. Sun, W. Lin, G. Yi, Q. Li, *Adv. Sci.* **2024**, *11*, 2401983.
[40] D. Bukharina, L. Southard, B. Dimitrov, J. A. Brackenridge, S. Kang, P. Min, Y. Wang, D. Nepal, M. E. McConney, T. J. Bunning, N. A. Kotov, V. V. Tsukruk, *Adv. Funct. Mater.* **2024**, 2404857.
[41] B. Dimitrov, D. Bukharina, V. Poliukhova, D. Nepal, M. E. McConney, T. J. Bunning, V. V. Tsukruk, *ACS Appl. Opt. Mater.* **2024**, https://doi.org/10.1021/acsaom.4c00386
[42] M. E. McConney, S. Singamaneni, V. V. Tsukruk, *Polym. Rev.* **2010**, *50*, 235.
[43] K. Daicho, T. Saito, S. Fujisawa, A. Isogai, *ACS Appl. Nano Mater.* **2018**, *1*, 5774.
[44] W.-T. Cao, F.-F. Chen, Y.-J. Zhu, Y.-G. Zhang, Y.-Y. Jiang, M.-G. Ma, F. Chen, *ACS Nano* **2018**, *12*, 4583.
[45] Z. Zhan, Q. Song, Z. Zhou, C. Lu, *J. Mater. Chem. C* **2019**, *7*, 9820.
[46] Alexander, L. E. *X-Ray Diffraction Methods in Polymer Science*; Wiley-Interscience: New York, 1970.
[47] V. V. Tsukruk, V. V. Shilov, *Structure of Liquid Crystal Polymers*, Naukova Dumka, Kiev, 1990
[48] C. E. Shuck, A. Sarycheva, M. Anayee, A. Levitt, Y. Zhu, S. Uzun, V. Balitskiy, V. Zahorodna, O. Gogotsi, Y. Gogotsi, *Adv. Eng. Mater.* **2020**, *22*.
[49] T. Starkey, P. Vukusic, *Nanophotonics* **2013**, 2, 289.
[50] S. Kinoshita, S. Yoshioka, *ChemPhysChem* **2005**, *6*, 1442.
[51] T. Smith, J. Guild, *Trans. Opt. Soc., London* **1931**, *33*, 73.
[52] T. Young, *Philos. Trans. R. Soc. London* **1802**, *92*, 12.
[53] C. Oleari, in *Optical Thin Films and Coatings* (Eds: A. Piegari, F. Flory), Woodhead Publishing, Sawston, United Kingdom, **2013**, Ch. 9.
[54] B. Zhu, V. E. Johansen, G. Kamita, G. Guidetti, M. M. Bay, T. G. Parton, B. Frka-Petesic, S. Vignolini, *ACS Nano* **2020**, *14*, 15361.
[55] V. V. Vogler-Neuling, M. Saba, I. Gunkel, J. O. Zoppe, U. Steiner, B. D. Wilts, A. Dodero, *Adv. Funct. Mater.* **2024**, *34*, 2306528.
[56] B. Frka-Petesic, T. G. Parton, C. Honorato-Rios, A. Narkevicius, K. Ballu, Q. Shen, Z. Lu, Y. Ogawa, J. S. Haataja, B. E. Droguet, R. M. Parker, Silvia Vignolini, *Chem. Rev.* **2023**, *123*, 12595.
[57] A. D. Dillon, M. J. Ghidiu, A. L. Krick, J. Griggs, S. J. May, Y. Gogotsi, M. W. Barsoum, A. T. Fafarman, Highly Conductive Optical Quality Solution-Processed Films of 2D Titanium Carbide, *Adv. Funct. Mater.*, **26**, 4162-4168 (2016)
[58] S. Tadepalli, J. M. Slocik, M. K. Gupta, R. R. Naik, S. Singamaneni, *Chem. Rev.* **2017**, *117*, 12705.
[59] S. Kinoshita, S. Yoshioka, *ChemPhysChem* 2005, 6, 1442.